remote sensing

MDPI

Article

Simulation of Spectral Albedo and Bidirectional Reflectance over Snow-Covered Urban Canyon: Model Development and Factor Analysis

Qi-Xiang Chen [1,*,†], Zi-Yi Gao [1,†], Chun-Lin Huang [1], Shi-Kui Dong [1] and Kai-Feng Lin [2]

[1] School of Energy Science and Engineering, Harbin Institute of Technology, No.92 Xidazhi Street, Harbin 150001, China; 20b902039@stu.hit.edu.cn (Z.-Y.G.); 20b902059@stu.hit.edu.cn (C.-L.H.); dongsk@hit.edu.cn (S.-K.D.)
[2] School of Chemistry and Chemical Engineering, Harbin Institute of Technology, No.92 Xidazhi Street, Harbin 150001, China; linkaifeng@hit.edu.cn
* Correspondence: atlas.chen@hit.edu.cn
† These authors contributed equally to this work.

Abstract: A critical comprehension of the impact of snow cover on urban bidirectional reflectance is pivotal for precise assessments of energy budgets, radiative forcing, and urban climate change. This study develops a numerical model that employs the Monte Carlo ray-tracing technique and a snow anisotropic reflectance model (ART) to simulate spectral albedo and bidirectional reflectance, accounting for urban structure and snow anisotropy. Validation using three flat surfaces and MODIS data (snow-free, fresh snow, and melting snow scenarios) revealed minimal errors: the maximum domain-averaged BRDF bias was 0.01% for flat surfaces, and the overall model-MODIS deviation was less than 0.05. The model's performance confirmed its accuracy in reproducing the reflectance spectrum. A thorough investigation of key factors affecting bidirectional reflectance in snow-covered urban canyons ensued, with snow coverage found to be the dominant influence. Urban coverage, building height, and soot pollutant concentration significantly impact visible and infrared reflectance, while snow grain size has the greatest effect on shortwave infrared. The bidirectional reflectance at backward scattering angles (0.5–0.6) at 645 nm is lower than forward scattering (around 0.8) in the principal plane as snow grain size increases. These findings contribute to a deeper understanding of snow-covered urban canyons' reflectance characteristics and facilitate the quantification of radiation interactions, cloud-snow discrimination, and satellite-based retrieval of aerosol and snow parameters.

Keywords: urban canyon; snow cover; bidirectional reflectance; Monte Carlo simulation; ART

check for updates

Citation: Chen, Q.-X.; Gao, Z.-Y.; Huang, C.-L.; Dong, S.-K.; Lin, K.-F. Simulation of Spectral Albedo and Bidirectional Reflectance over Snow-Covered Urban Canyon: Model Development and Factor Analysis. *Remote Sens.* **2024**, *16*, 2340. https://doi.org/10.3390/rs16132340

Academic Editors: Diego González-Aguilera and Pablo Rodríguez-Gonzálvez

Received: 18 April 2024
Revised: 24 June 2024
Accepted: 24 June 2024
Published: 27 June 2024

Copyright: © 2024 by the authors. Licensee MDPI, Basel, Switzerland. This article is an open access article distributed under the terms and conditions of the Creative Commons Attribution (CC BY) license (https://creativecommons.org/licenses/by/4.0/).

1. Introduction

The world has undergone a dramatic process of urbanization, with half of the world's population living in urban areas [1] and more than 600 million people now living in winter cities located above 45° worldwide [2]. Man-made urban surfaces (e.g., concrete pavements, buildings, and asphalt roads) generally have higher surface reflectance than natural surfaces (e.g., grass, forest, and wetlands). Long-term snow cover over urban canyons during wintertime further increases urban surface reflectance and redistributes the radiation budget [3,4], and urbanization-induced emissions of anthropogenic pollutants and enhanced anthropogenic heating together lead to varying degrees of impact on local weather, environment, and climate [5]. Therefore, it is important to clarify the influence of snow cover on the reflectivity of urban canyons for a better understanding of the urban climate system.

In addition, snow-covered surfaces are also a great challenge for aerosol remote sensing [6]. Snow cover over urban canyons creates strong heterogeneity and different reflectivity characteristics compared to snow-free urban canyons and flat snow surfaces,

and processes such as pollutant deposition, snow grain aging, and snow melting further change their directional reflectivity characteristics [3,7]. Separating and explicitly describing the aerosol contributions from the top-of-atmosphere (TOA) radiance measured by satellite-based instruments is at the core of aerosol remote sensing, but it is still challenging because the contribution of highly reflective snow-covered surfaces is much higher than that of aerosol, which could easily lead to unacceptable inversion bias [8]. Therefore, a thorough understanding of the influence of snow cover on the reflectance of urban canyons is essential for further improvements in aerosol remote sensing in winter cities.

The bidirectional reflectance distribution function (BRDF) is a critical factor in aerosol remote sensing, radiative forcing, and albedo feedback [9,10]. The BRDF model has the potential to reduce errors in mapping snow-covered areas, separating snow from clouds, and retrieving aerosol optical depth (AOD) [11]. For example, Ji et al. [12] collected and compared the differences in BRDF between pure snow, pure ice, and ice-snow to support snow/ice/ice-snow classification and monitoring. Gatebe and King [13] established an airborne BRDF database of snow, cloud, and other major surface types over a 30-year period (1984–2014) to support snow/cloud discrimination and various remote sensing applications. Tian et al. [14] and Lin et al. [15] reported the potential use of BRDF in improving the quality of AOD retrieval over urban areas.

Efforts in remote sensing of aerosols over the cryosphere using snow BRDF have been reported in many previous studies [6,16]. For example, Shi et al. [17] used the dual-angle observation of AATSR to perform AOD inversion in the Arctic region, and the correlation coefficients between the inversion results and the ground-based observations were 0.75 and 0.70, respectively. Mei et al. [8] improved the XBAER inversion algorithm to achieve AOD inversion over the cryosphere, which assumes that the surface reflectance can be characterized by a one-dimensional linear equation, and the regression coefficients are stored in a pre-calculated database based on a large number of observations. Swain et al. [18] retrieved the AOD over snow-covered regions of the Arctic using passive remote sensing from space, and the surface reflectance was parameterized by a two-parameter snow BRDF model [19].

Research on snow BRDF models to support AOD inversion in polar regions has made good progress, but little has been reported on AOD inversion over snow-covered urban canyons. Establishing an accurate BRDF database to support AOD inversion, as Deep Blue [20], Dark Target [21], and XBAER algorithms [8] have previously done, is a challenging task. Compared with polar and alpine mountain environments, snow in winter cities is more often affected by aerosol deposition contamination, as well as grain aging and melting, resulting in continuous changes in reflectance properties [22]. Zhang et al. [23] reported that the deposition of black carbon and sandy aerosol particles led to a 20% decrease in snow albedo in the southeastern region of the Qinghai-Tibetan Plateau. Wang et al. [24] found that snow albedo decreased by 2–6% due to BC contamination with 100–500 ng/g^{-1} BC in the snowpack. Thus, the surface reflectance database constructed under the assumption of short-term invariance cannot accurately characterize the time series variations of the snow-covered urban canyon BRDF, resulting in the lack of winter AOD products over high latitude cities. The lack of in-depth understanding of the effect of snow on the spectral albedo and BRDF characteristics over the urban canyon is considered to be the primary factor.

Motivated by the need for BRDF characteristics over snow-covered urban canyons, we attempt to develop a new snow-covered urban bidirectional reflectance model to comprehensively evaluate the effect of snow cover on urban reflectance. This model is established based on the Monte Carlo ray tracing method, which has been widely used and validated to simulate directional reflectance over rugged terrain [25–27] and terrestrial snow [28–30]. The asymptotic radiative transfer (ART) model is applied to simulate the bidirectional reflectivity characteristics of snow, since the ART model has been extensively validated to retrieve the snow grain size, pollutant concentration, and snow albedo [31–33]. This study is organized as follows. Section 2 gives detailed descriptions of the data and

methods used, including Monte Carlo ray tracing and the ART model. Section 3 presents the model validation, and Section 4 gives further assessments of the influence of key factors on urban BRDF. Section 5 gives a brief conclusion and prospects.

2. Materials and Methods

2.1. Site Description

Harbin, often referred to as the "Ice City" of China, is the provincial capital of Heilongjiang and is situated in the northernmost part of the Northeast China Plain (Figure 1a). With a temperate continental monsoon climate featuring approximately four months of snow cover [34,35], Harbin is a megacity spanning over 10,200 square kilometers and home to approximately 10.7 million permanent residents [36]. Given its prolonged snow cover and moderate air pollution [37,38], we selected this region (125°42′E–130°10′E, 44°04′N–46°40′N) to validate our numerical model. Figure 1c–e shows the corresponding spectral albedo map on 13 October 2019 (autumn season). The domain-averaged albedos at 645 nm, 469 nm, and 1640 nm are 0.098, 0.053, and 0.220, respectively. In Figure 1e, the Songhua River and urban areas stand out with lower reflectance in the shortwave infrared bands compared to the surrounding vegetation.

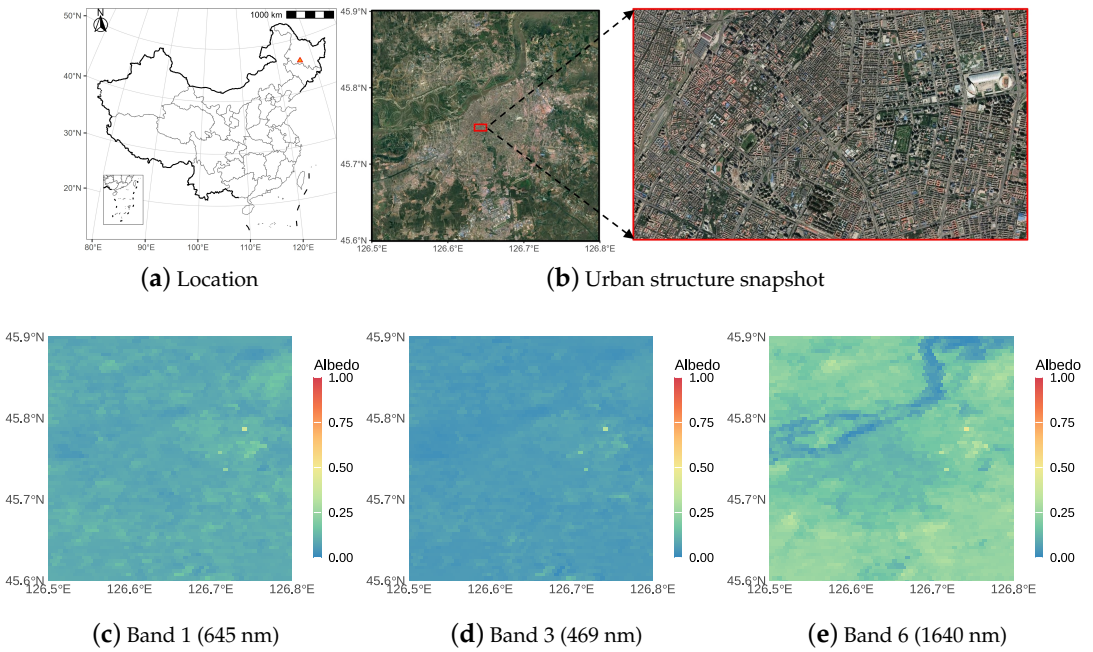

(**a**) Location (**b**) Urban structure snapshot

(**c**) Band 1 (645 nm) (**d**) Band 3 (469 nm) (**e**) Band 6 (1640 nm)

Figure 1. (**a**) The location of Harbin, situated in northeastern China, and (**b**) image taken from the EOSDIS Worldview website (https://worldview.earthdata.nasa.gov/, accessed 17 June 2024), which showcases a snapshot of the urban structure. Distribution of spectral albedo (**c**–**e**) within the study area (126.5°E to 126.8°E, 45.6°N to 45.9°N), with data derived from the MODIS Terra MOD09A1 product on 13 October 2019 (autumn season).

2.2. Geometric Modeling of Urban Canyons

Considering the variations in urban architecture, such as commercial centers, residential zones, and factories, we design an urban canyon model with a 25% building coverage to accurately represent the urban layout and ensure numerical simulations are representative. The urban canyon, measuring 2.5 km by 2.5 km, is divided into a 50 × 50 m grid in both the x and y directions. Building heights are assumed to follow a normal distribution, with an average of 50 m and a standard deviation of 0.6. The three-dimensional representation of the urban canyon is displayed in Figure 2.

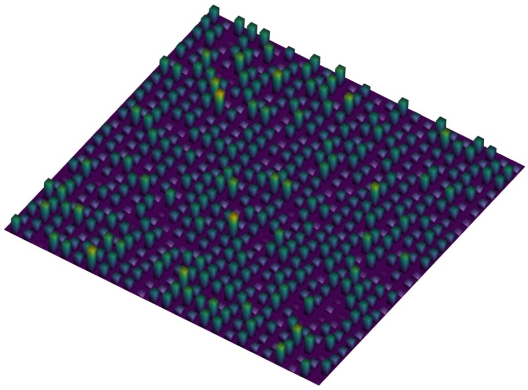

Figure 2. The topographical representation of the modeled urban canyons configured with standard parameters.

The geometric modeling defaults and their variation ranges for urban canyons and snow are detailed in Table 1. The default parameters include a building coverage (BC) of 25%, a building height (BH) of 50 m, a solar zenith angle (SZA) of 70°, and a relative azimuth angle of 0°. To investigate the impact of varying building structure and snow conditions on spectral albedo and BRDF properties, we consider the following ranges: building coverage from 10% to 50%, building height between 10 m and 90 m with a standard deviation of 0.6, solar zenith angle ranging from 40° to 80° in increments of 10°, and relative azimuth angle varying from 0° to 180°.

For snow, we focus on snow coverage (SC), snow grain size (SGS), and soot pollutant concentration (SPC). The initial settings are 80% snow coverage, 3600 µm snow grain size, and a soot pollutant concentration of 500 ppb. In our analysis, snow coverage varies between 20% and 100%, snow grain size ranges from 100 µm to 5000 µm, and soot pollutant concentrations span from 10^2 ppb to 10^6 ppb.

Table 1. Input parameters of the numeric model.

Parameter	Unit	Range	Default
building coverage	-	10–50%	25%
building height	meter	10–90	50
length of x	km	-	2.5
length of y	km	-	2.5
snow coverage	-	20–100%	80%
snow grain size	µm	1000–5000	3600
pollutant concentration	ppb	10^2–10^6	500
zenith angle	degree	40–80	70
azimuth angle	degree	0–180	0

2.3. Satellite Albedo Product

The Terra MOD09A1 and Aqua MYD09A1 Version 6 Moderate Resolution Imaging Spectroradiometer (MODIS) products provide surface spectral albedo estimates for Bands 1 through 7 (as listed in Table 2). These data have been meticulously corrected for atmospheric influences, such as gases, aerosols, and Rayleigh scattering. For each pixel, the most suitable observation within an eight-day composite period is chosen based on cloud cover and solar zenith angle. In cases where multiple acquisitions meet the criteria, the pixel with the lowest Band 3 (blue) value is selected. This choice represents the optimal Level 2G (L2G) observation, which maximizes coverage, avoids clouds and cloud shadows, and minimizes aerosol effects. The Collection 6 surface reflectance product exhibits an accuracy of at least 0.005 + 0.05 SR across all bands, where SR denotes surface reflectance [39].

Table 2. Band information of the MODIS albedo product.

Band	Wavelength	Spectra
Band 1	620–670 nm	Red
Band 2	841–876 nm	NIR
Band 3	459–479 nm	Blue
Band 4	545–565 nm	Green
Band 5	1230–1250 nm	SWIR
Band 6	1628–1652 nm	SWIR
Band 7	2105–2155 nm	SWIR

The MODIS spectral albedo is derived from an operational algorithm that integrates the RossThick–LiSparseReciprocal (RTLSR) semi-empirical model for inversion [40,41]. This model decomposes the bidirectional reflectance distribution function (BRDF) into a weighted sum of an isotropic component (f_{iso}) and two distinct kernels. One, K_{vol}, is based on volume scattering radiative transfer models, while the other, K_{geo}, is informed by surface scattering and geometric shadow casting theory [42]. The operational product computes BRDF parameters (f_{iso}, f_{vol}, f_{geo}) that are spectrally dependent weights assigned to each kernel for calculating the overall anisotropic reflectance. Figure 3 illustrates the viewing geometry and planes, including the principal plane (PP), cross plane (CP), and almucantar plane (ALM).

$$\begin{aligned} R(\theta_s, \theta_v, \varphi, \lambda) =& f_{iso}(\lambda) \\ &+ f_{geo}(\lambda) K_{geo}(\theta_s, \theta_v, \varphi) \\ &+ f_{vol}(\lambda) K_{vol}(\theta_s, \theta_v, \varphi), \end{aligned} \tag{1}$$

where θ_s, θ_v, φ, and λ represent the solar zenith angle, view zenith angle, relative azimuth angle, and wavelength, respectively. $K_{geo}(\theta_s, \theta_v, \varphi)$ and $K_{vol}(\theta_s, \theta_v, \varphi)$ are the geometric optical kernel and the volume scattering kernel, respectively. f_{iso}, f_{geo}, and f_{vol} represent the weight coefficients of isotropical kernel (equal to 1), geometric optical kernel, and scattering kernel with wavelength λ, respectively. The RossThick volume scattering kernel and the LiSparseReciprocal geometric optical kernel are formulated as follows:

$$\begin{aligned} K_{geo}(\theta_s, \theta_v, \varphi) =& \mathrm{O}(\theta_s, \theta_v, \varphi) - \sec\theta_s - \sec\theta_v + \\ & \frac{1}{2}(1 + \cos\xi) \sec\theta_v \sec\theta_s \end{aligned} \tag{2}$$

$$K_{vol}(\theta_s, \theta_v, \varphi) = \frac{(\pi/2 - \xi)\cos\xi + \sin\xi}{\cos\theta_s + \cos\theta_v} - \frac{\pi}{4}, \tag{3}$$

where $\mathrm{O}(\theta_s, \theta_v, \varphi)$ is the overlap function of the viewing and sunlit shadows, and ξ refers to the phase angle regarding the viewing and illuminating geometries [42].

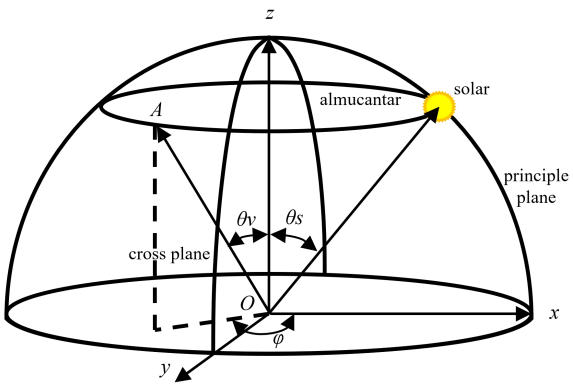

Figure 3. Viewing geometry and plane definitions.

To facilitate urban pixel extraction, a 500-meter land cover dataset is utilized. The MCD12Q1 Version 6 data product, which offers annual land cover classifications, is derived from MODIS Terra and Aqua reflectance data through supervised classification methods [43]. The International Geosphere-Biosphere Programme (IGBP) legend is employed to identify urban areas. This classification scheme consists of 18 categories, with urban and built-up lands designated as Class 13. This classification is based on the presence of at least 30% impervious surface area, including buildings, asphalt, and vehicles [44,45].

2.4. Snow ART Model

Snow is primarily composed of ice crystals. Upon interaction with sunlight, these crystals predominantly reflect photons due to their icy surfaces, which then undergo reflection and refraction. The ART model, based on the concept of fractal particles, estimates snow reflectance by considering the influence of soot pollution and the size of snow grains. The bidirectional reflectance of snow is approximated using an exponential function [19,46]:

$$r_{so} = r_0 exp\left(\frac{-\alpha K_s K_v}{r_0}\right) \tag{4}$$

$$K_s = \frac{3}{7}(1 + 2cos\theta_s') \tag{5}$$

$$K_v = \frac{3}{7}(1 + 2cos\theta_v') \tag{6}$$

$$r_0 = \frac{a + b(cos\theta_s' + cos\theta_v') + c \cdot cos\theta_s' cos\theta_v' + p}{4(cos\theta_s' + cos\theta_v')} \tag{7}$$

$$p = 11.1exp(-0.087\Theta) + 1.1exp(-0.014\Theta) \tag{8}$$

$$cos\Theta = -cos\theta_s' cos\theta_v' + \sin\theta_s' \sin\theta_v' \cos(\varphi_s' - \varphi_v') \tag{9}$$

$$\alpha = A\sqrt{\frac{4\pi a_{ef}}{\lambda}(k + C_{soot})}, \tag{10}$$

where θ_s' and θ_v' are relative solar zenith angle and relative view zenith angle, respectively. K_s and K_v are the escape functions for different relative solar zenith angles and view zenith angles, respectively. r_0 is the reflectance of zero absorption medium, while a, b, and c equal 1.247, 1.186, and 5.157, respectively. φ_s' and φ_v' are the relative solar and view azimuth angle, respectively. Θ is the scattering angle. A is equal to 5.8, while a_{ef} and C_{soot} are snow grain size and pollutant concentration, respectively. k is related to the ice refractive index [11,46]. The spectral reflectance of snow using default values of snow grain and soot pollutant concentration is shown in Figure 4.

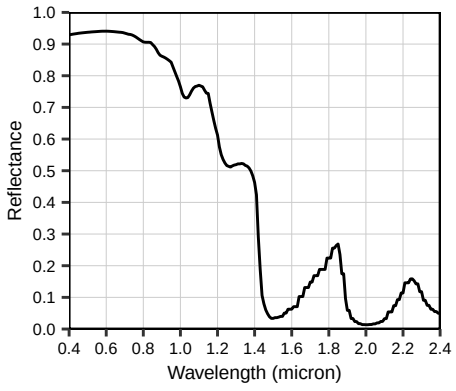

Figure 4. The spectral reflectance of snow as simulated by the ART model for MODIS Band 1 (469 nm), with a snow grain size of 3600 µm and a soot pollutant concentration of 500 ppb.

2.5. Spectral Albedo Data for Urban Surfaces

The spectral reflectance data for urban surfaces were sourced from the United States Geological Survey (USGS) Spectral Library version 7 (https://www.usgs.gov/labs/spectroscopy-lab/science/spectral-library, accessed on 1 April 2024), which contains thousands of laboratory-measured spectra of minerals, vegetation, and man-made materials [47]. Covering wavelengths from 0.2 µm to 200 µm, the library facilitates the understanding of remotely sensed data by linking spectral features to chemical structures. In this research, we employed eight man-made materials (brushed aluminum, asphalt road, asphalt shingle, asphalt tar, concrete road, concrete surface, painted aluminum, and roofing felt) and three natural materials (snow melt, aspen leaves, and gray pine branches). Their respective spectral reflectances are displayed in Figure 5.

We assume that, under normal conditions, a building roof typically consists of brushed aluminum (30%), asphalt shingle (10%), asphalt tar (10%), painted aluminum (30%), and roofing felt (20%). The ground surface is composed of aspen leaves (10%), asphalt road (10%), concrete road (50%), and gray pine (30%). When snow covers both the roof and ground, the roof is primarily snow (80%), with brushed aluminum (10%) and painted aluminum (10%) contributing, while the ground surface consists of snow (70%), asphalt road (5%), gray pine (5%), and concrete road (20%). The building facade is characterized by a concrete surface.

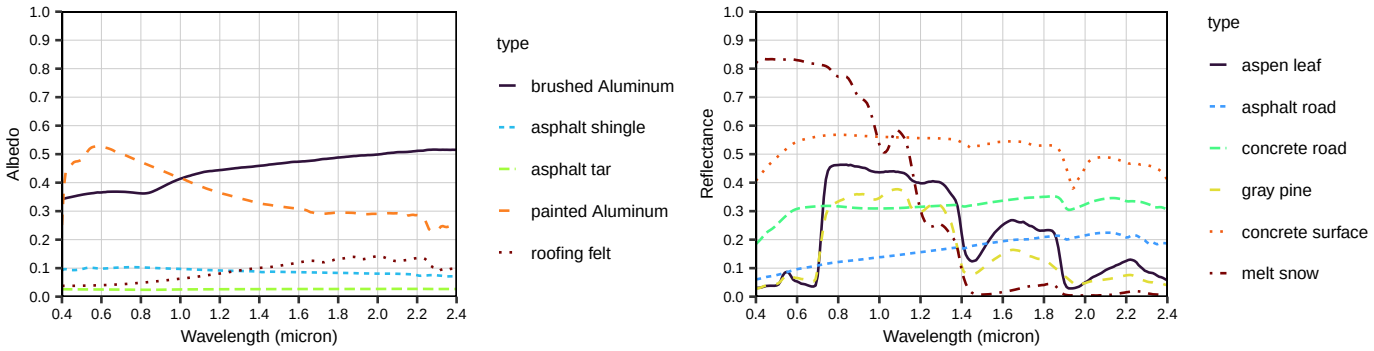

Figure 5. Spectral albedo of selected man-made and natural materials.

2.6. Monte Carlo Ray-Tracing Method

The Monte Carlo ray-tracing method, a versatile approach for solving the radiative transfer equation in complex environments like urban canyons with diverse surface properties (roofs, ground, and facades) [48,49], accurately models the domain-averaged albedo and bidirectional reflectance distribution function (BRDF) over snow-covered canyons by simulating 3D photon transport. The core principle of this technique involves simulating photon interactions with surfaces, accounting for reflection. Note that the proposed model disregards absorption and scattering by atmospheric particles [50].

Beginning with a photon's energy, position, and direction, the process entails the following steps: upon entering the domain from the solar incidence direction, the photon's intersection with a surface is identified. Once the reflection point is known, the new photon direction is determined based on the local BRDF, and the photon's weight is adjusted according to the surface albedo. This iterative process continues until the photon exits the physical boundaries or is fully absorbed. The overall albedo is calculated as the ratio of outgoing to incoming photon energy (as depicted in Figure 6), and the BRDF is derived accordingly:

$$\begin{aligned} \mathrm{BRDF} &= \frac{\pi M_r(\Omega_r)}{M_0 \Omega_r cos\theta_r} \\ &= \frac{\pi M_r(\Omega_r)}{M_0 cos\theta_r sin\theta_r d\theta_r d\varphi} \end{aligned} \tag{11}$$

$$d\Omega = \frac{dA}{r^2} = sin\theta d\theta d\varphi, \tag{12}$$

where Ω_r represents the reflection direction, $M_r(\Omega_r)$ is the energy of outgoing photons at θ_r and φ, M_0 is the total incident energy, and Ω represents the solid angle. In the urban canyon, surfaces are primarily characterized by Lambertian properties, while snow cover exhibits anisotropic behavior according to the RTLSR model. For multi-component roof and ground surfaces, the surface albedo ρ and bidirectional reflectance distribution function (BRDF) are calculated by considering the albedo weighting:

$$\rho = \frac{\sum \eta_i \rho_i}{\sum \rho_i} \tag{13}$$

$$\text{BRDF} = \frac{\sum \eta_i \text{BRDF}_i}{\sum \text{BRDF}_i}, \tag{14}$$

where η_i represents the area share of the ith surface.

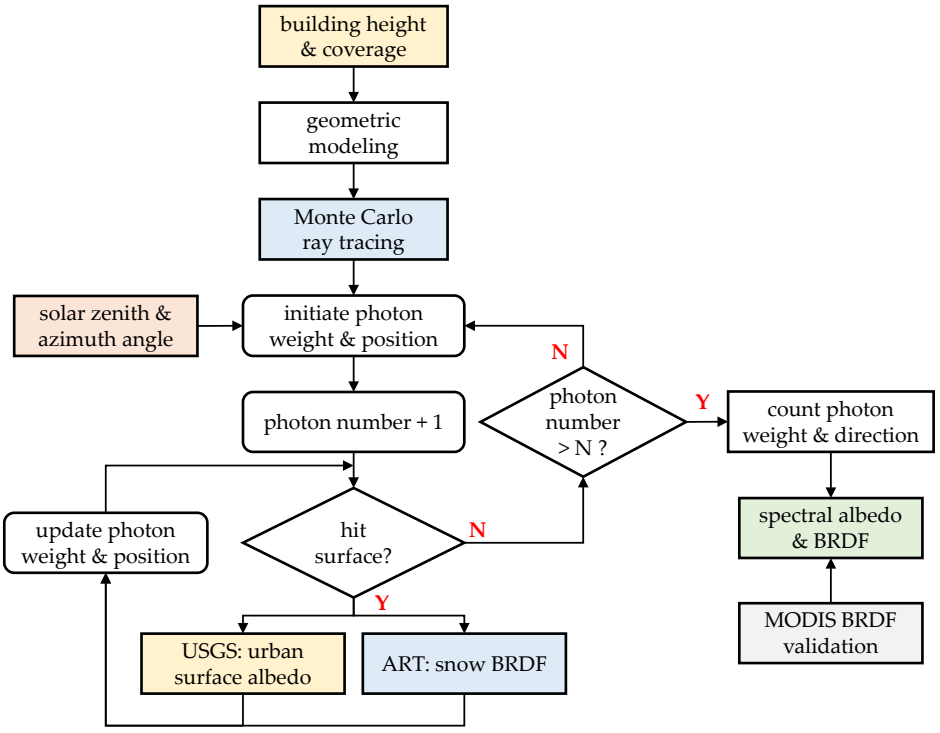

Figure 6. Flowchart of the proposed snow-covered urban BRDF model.

3. Model Validation

3.1. Validation over Flat Surfaces

To evaluate the model performance, we compare the Monte Carlo-generated albedo to the exact value for a flat Lambertian surface with an albedo of 0.2 under a solar zenith angle of 45°. The surface, measuring 2.5 km by 2.5 km, is divided into a 50 × 50 grid with 50-m intervals in both x and y directions. Figure 7 demonstrates the trend of domain-averaged relative error as a function of incident photon count. It is clearly shown that the simulation error decreases as the photon count increases. The modeled BRDF exhibits a relative error of 0.75% and 0.49% when using 10^7 and 10^8 photons, respectively. To strike a balance between accuracy and computational efficiency, we opt for 10^7 photons for further simulations.

In Figure 8, a comparison of modeled BRDF distributions is shown with respect to established distributions for a flat Lambertian surface and two anisotropic surfaces. The analysis is based on MODIS Band 3 at a wavelength of 469 nm. The anisotropic surfaces

are characterized by the RTLSR, model with $f_{iso} = 0.091$, $f_{vol} = 0.032$, and $f_{geo} = 0.012$, and the ART model with a snow grain size of 500 µm and a soot pollutant concentration of 3600 ppb. The domain-averaged albedos for the Lambertian, RTLSR, and ART surfaces are 0.199, 0.078, and 0.914, respectively, with corresponding relative biases of −0.49%, −1.57%, and −0.13%. The maximum biases across all cases do not exceed 0.01%, while the maximum relative biases are within 2% for the Lambertian, 5% for the RTLSR, and 3% for the ART surfaces. These results indicate that the numerical model performs admirably in flat surface scenarios.

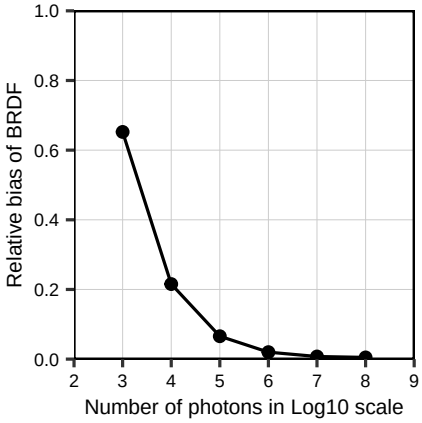

Figure 7. Variations of domain-averaged relative error with incident photon numbers.

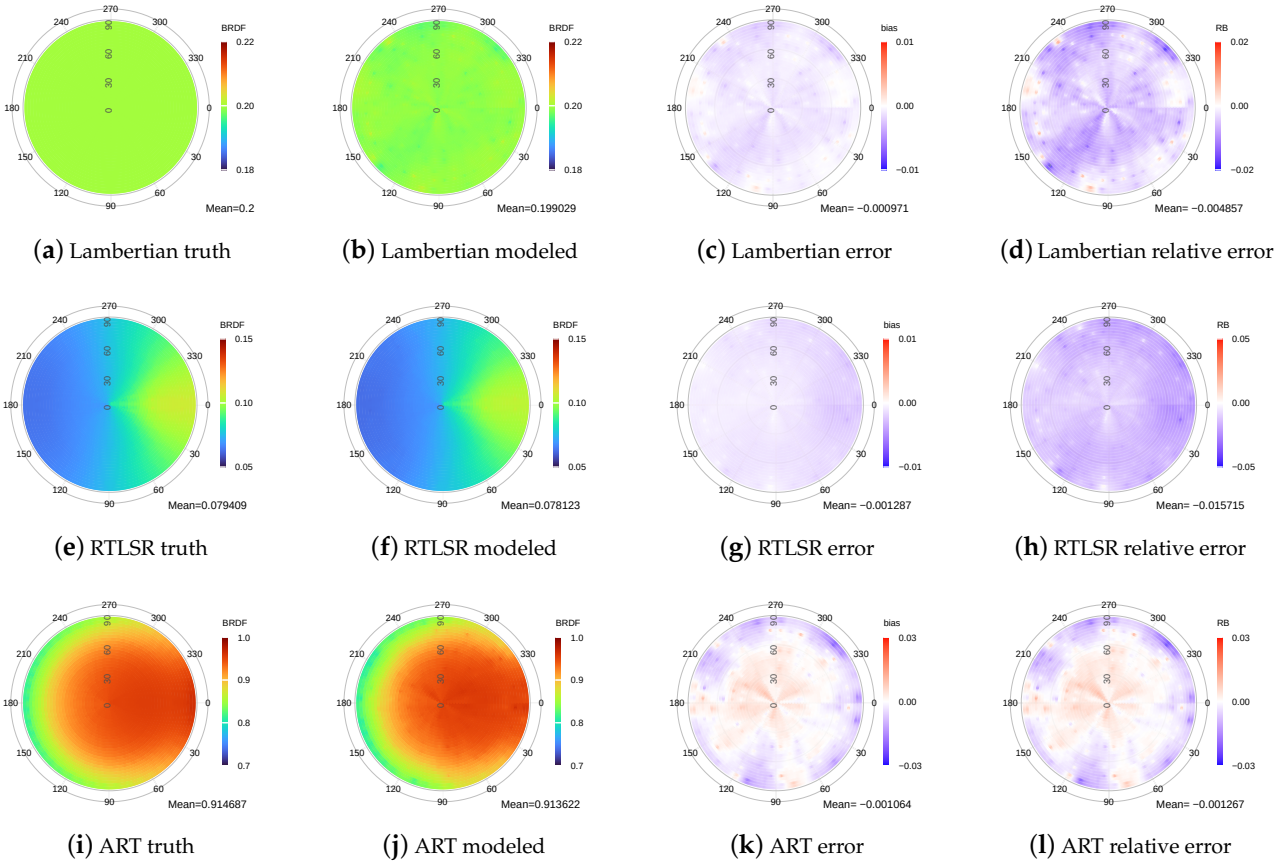

(**a**) Lambertian truth (**b**) Lambertian modeled (**c**) Lambertian error (**d**) Lambertian relative error

(**e**) RTLSR truth (**f**) RTLSR modeled (**g**) RTLSR error (**h**) RTLSR relative error

(**i**) ART truth (**j**) ART modeled (**k**) ART error (**l**) ART relative error

Figure 8. Comparisons of simulated BRDF with truth values over flat Lambertian, RTLSR, and ART surfaces. Solar zenith angle is 45°; Lambertian albedo is 0.2; RTLSR model coefficients are $f_{iso} = 0.091$, $f_{vol} = 0.032$, and $f_{geo} = 0.012$; and the ART model has a snow grain size of 500 µm and pollutant concentration of 3600 ppb.

3.2. Validation with MODIS Albedo Observations

Figure 9 illustrates the time series of spectral albedo for Band 1 (red), Band 3 (blue), and Band 6 (SWIR). Winter exhibits significantly higher albedos compared to other seasons, persisting for over four months. The mean spectral albedo at Band 1 (645 nm) is approximately 0.4 during winter, with a minimal difference between the MODIS Terra and Aqua measurements. Band 3 (469 nm) shows more pronounced variations, while the albedo at Band 6 (1640 nm) exhibits a contrasting pattern, with low values in winter (around 0.1) and higher values in the rest of the year (approximately 0.2). These spectral patterns are closely linked to snow cover, as snow reflects strongly in visible and infrared bands but has a lower reflectance in the shortwave infrared band (as depicted in Figures 4 and 5).

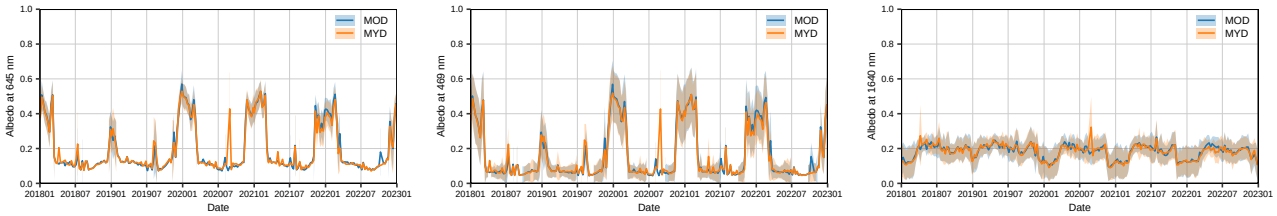

(**a**) Band 1 (645 nm) (**b**) Band 3 (469 nm) (**c**) Band 6 (1640 nm)

Figure 9. Time series of spectral albedos from the MOD09/MYD09 dataset over Harbin between 2018 and 2022.

To thoroughly assess the model's performance, three MODIS dataset scenarios were extracted: snow-free, fresh snow, and snow melt. These scenarios were employed to evaluate if the numerical model could accurately reproduce observed spectral albedos. The analysis focused on Harbin, and only pixels with IGBP land cover types of urban and built-up are considered. Figure 10 illustrates the spectral changes in MOD09, MYD09, and modeled albedo for each condition. On 11 November 2019, Harbin was in the early winter with no recent snowfall, showing a lower visible band albedo compared to infrared and shortwave bands. A snowfall on 28 December 2019 led to a significant increase in surface albedo across all bands. By 11 February 2020, after a week without fresh snow, the visible band albedo decreased to around 0.35–0.40, remaining notably higher than the snow-free period. The model accurately captures the spectral albedo variations across these scenarios. As seen in Figure 10d–f, the model's deviation from observations is generally smaller than the discrepancies between the MOD09 and MYD09 data. The overall deviation between the model and observations does not exceed 0.05 for these scenarios, suggesting that the model effectively simulates spectral albedo and exhibits minimal deviation from real-world observations.

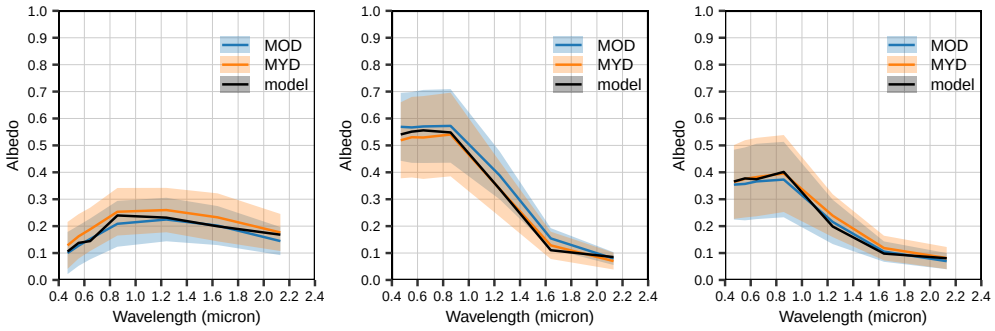

(**a**) Snow-free (2019-11-10) (**b**) Fresh snow (2019-12-28) (**c**) Snow melt (2020-02-11)

Figure 10. *Cont.*

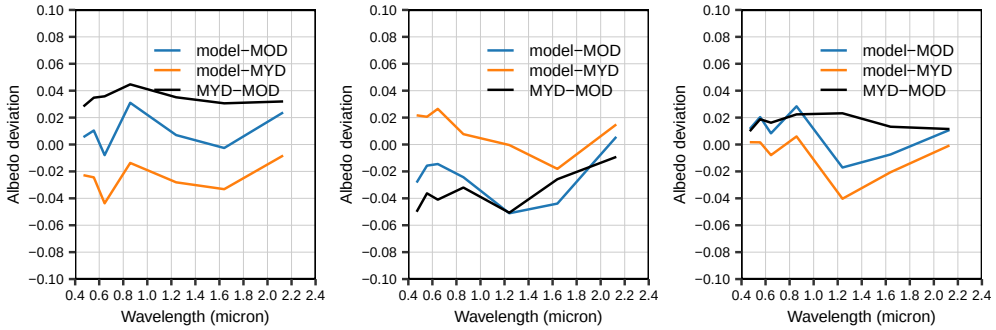

(**d**) Snow-free (2019-11-10) (**e**) Fresh snow (2019-12-28) (**f**) Snow melt (2020-02-11)

Figure 10. Spectral variations and deviations of MOD, MYD, and modeled albedos under snow-free, fresh snow, and snow melt scenarios.

4. Results

This section presents a comprehensive analysis of spectral albedo and bidirectional reflectance in relation to a number of key factors, including building coverage (BC), building height (BH), snow coverage (SC), snow grain size (SGS), soot pollutant concentration (SPC), and solar zenith angle (SZA). The default input variables presented in Table 1 are employed in this analysis.

4.1. Building Coverage

The influence of building coverage on the snow-covered urban canyon's albedo spectrum and bidirectional reflectance is showcased in Figure 11. Surface albedo across the visible and near-infrared wavelengths (400–1000 nm) varies from 0.50 to 0.70, as the building coverage increases from 10% to 50%. In contrast, the albedo values in the shortwave infrared band (1600–2200 nm) exhibit a more limited range of 0.10 to 0.15. As depicted in Figure 11a, the surface albedo over snow-covered urban canyons decreases as building coverage rises from 10% to 50%. This decline is mainly due to the increased number of reflections between roofs, ground, and faceted surfaces, which reduces the total energy carried by escaping photons. Figure 11b,c display the bidirectional reflectance distributions at MODIS Band 1 (645 nm) and Band 6 (1640 nm) in the hemispherical space. The average albedos for Band 1 and Band 6 are 0.578 and 0.131, respectively. Both polar plots exhibit angular variation, with higher reflectance at large backward scattering angles compared to the domain average, while forward scattering angles show lower values. In contrast to the strong backward scattering in fresh snow on flat surfaces (Figure 8i), urban structures significantly impact the directional reflectance characteristics.

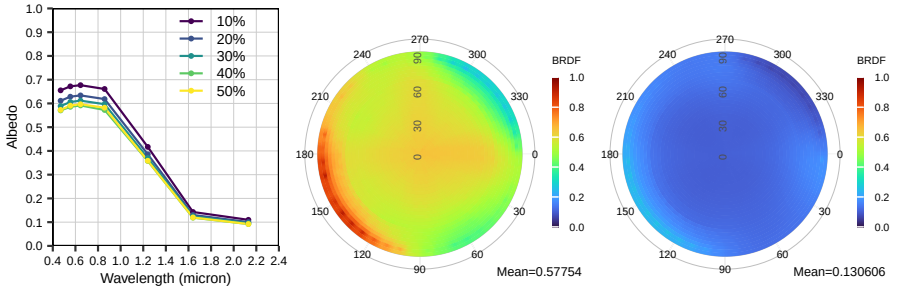

(**a**) (**b**) (**c**)

Figure 11. *Cont.*

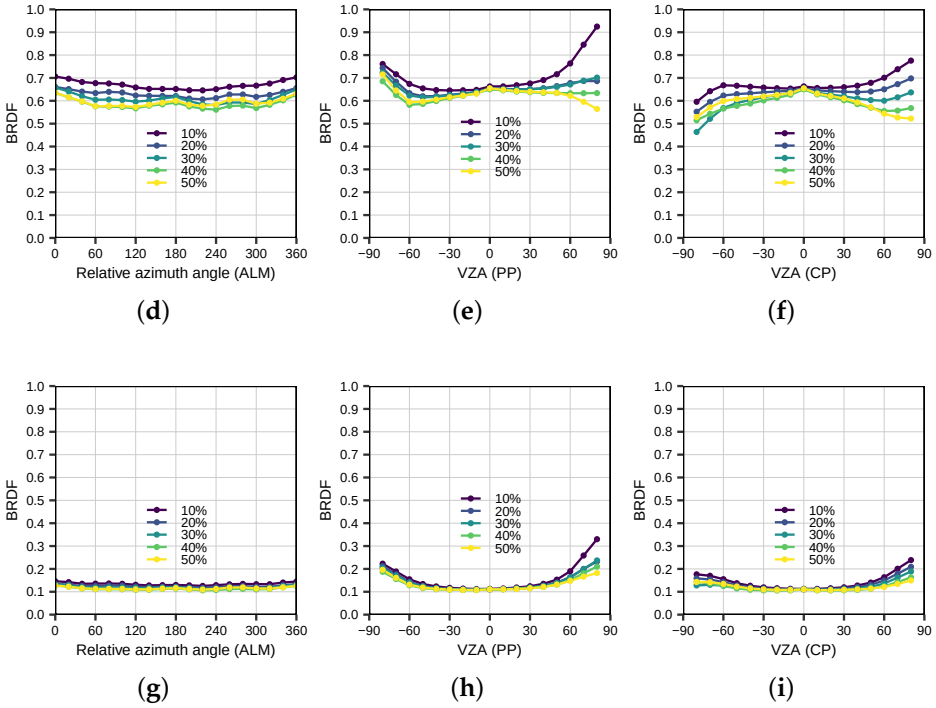

Figure 11. Spectral albedo and BRDF variations over urban canyons with building coverage varying from 10% to 50%. The negative VZA in the PP represents the direction of the relative azimuth angle of 180° (forward scattering direction), and the negative VZA in the CP represents the direction of the relative azimuth angle of 270°. (**a**) Spectral albedo. (**b**) BRDF distribution at Band 1 with BC = 50%. (**c**) BRDF distribution at Band 6 with BC = 50%. (**d**) ALM reflectance at Band 1. (**e**) PP reflectance at Band 1. (**f**) CP reflectance at Band 1. (**g**) ALM reflectance at Band 6. (**h**) PP reflectance at Band 6. (**i**) CP reflectance at Band 6.

The bidirectional reflectance changes with varying building coverages in ALM, PP, and CP are illustrated in Figure 11d–i. Reflectance variations at Band 1 are more pronounced than at Band 6. In the ALM, bidirectional reflectance is generally high at both forward and backward directions, with a slight dip between them. In the PP and CP, the impact of building coverage at a 0° view zenith angle (VZA) is minimal, and this effect increases with increasing VZA. The presence of buildings notably reduces backward scatter reflectance at higher VZA in the PP and CP. The PP's forward scattering reflectance shows a decreasing trend, followed by an increase with VZA, while the CP consistently exhibits a decreasing trend.

4.2. Building Height

Figure 12 demonstrates the influence of building height on snow-covered urban canyon albedo and bidirectional reflectance. As the height rises from 10 m to 90 m, a gradual decrease in spectral albedo across MODIS Bands 1–7 is noticeable. This decline tapers off with escalating height. In comparison to Figure 11, similar albedo levels are observed across the MODIS bands. Surface albedos in the visible and infrared regions fluctuate between 0.50 and 0.70, while those in the shortwave infrared range from 0.08 to 0.15. The lower albedo at higher building heights can be primarily attributed to enhanced interactions between photons and various surfaces, such as roofs, ground, and facades. Figure 12b,c display the bidirectional reflectance at Bands 1 and 6 in the hemispheric space for a 90-meter tall building. The domain-averaged reflectance at Bands 1 and 6 are 0.532 and 0.121, respectively. The angular variation in bidirectional reflectance is more pronounced with a building coverage ratio of 25% and a height of 90 m compared to a coverage of 50%

and a height of 50 m. This is evident from the bidirectional reflectance decrease at low VZA, while high VZA values exhibit more extreme values in both Band 1 and Band 6.

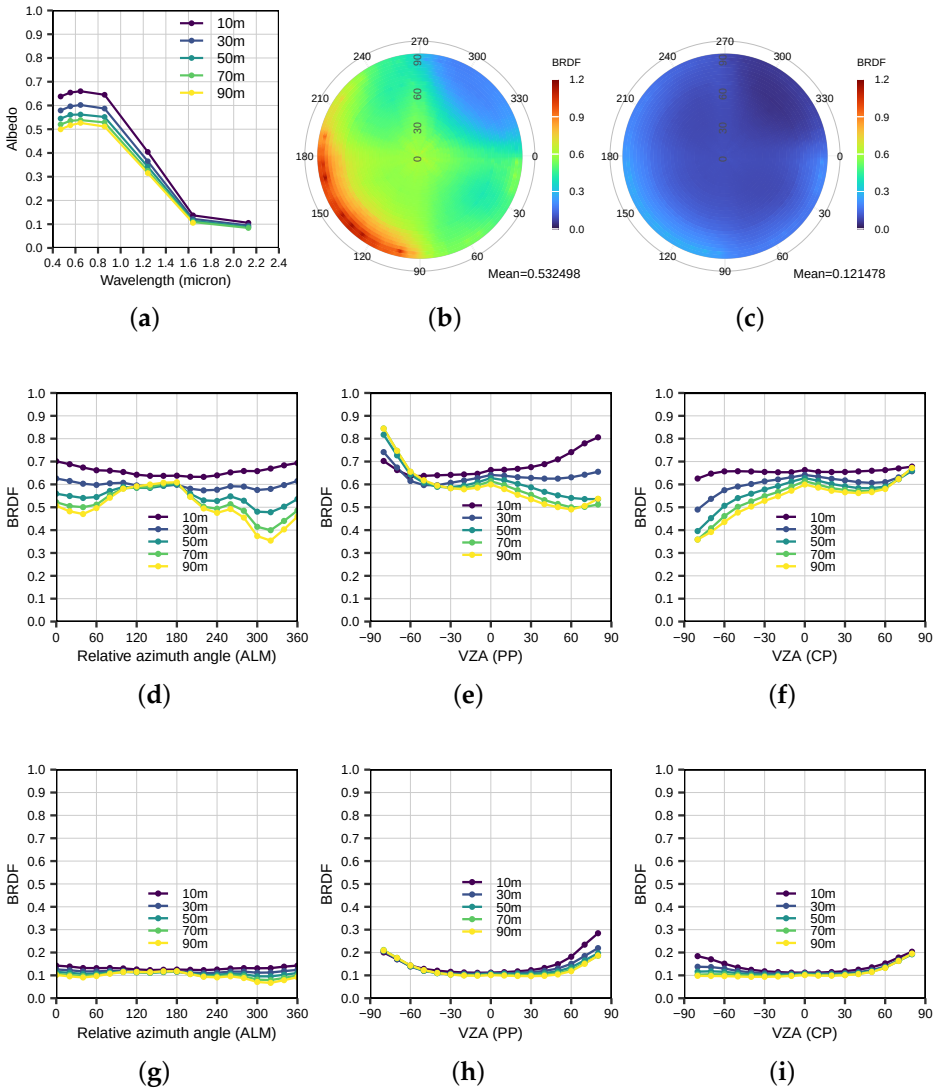

Figure 12. Spectral albedo and BRDF variations over urban canyons with building height varying from 10 m to 90 m. The negative VZA in the PP represents the direction of the relative azimuth angle of 180° (forward scattering direction), and the negative VZA in the CP represents the direction of the relative azimuth angle of 270°. (**a**) Spectral albedo. (**b**) BRDF distribution at Band 1 with BH = 90 m. (**c**) BRDF distribution at Band 6 with BH = 90 m. (**d**) ALM reflectance at Band 1. (**e**) PP reflectance at Band 1. (**f**) CP reflectance at Band 1. (**g**) ALM reflectance at Band 6. (**h**) PP reflectance at Band 6. (**i**) CP reflectance at Band 6.

The bidirectional reflectance changes with varying building heights in the ALM, PP, and CP are shown in Figure 12d–i. As the building height increases, the ALM exhibits less variation in reflectance between 120° and 180° relative azimuth angles, while backward scattering directions show greater variability. The reduction in reflectance due to height increase is more significant at the 240° to 360° angle compared to 0° to 120°. In the PP, backward scattering directions have significant variability, while forward scattering shows less. This variation decreases with increasing height. The CP displays a gradual rise in reflectance from forward to backward scattering, a trend linked to specific urban canyon structures. Given that our simulations employ a fixed default urban model (except in Section 3.1), the default bidirectional reflectance distribution is primarily determined by urban canyon characteristics. Although variations in urban structures can alter the pattern,

the focus on trends rather than absolute values or distributions enables a comprehensive understanding of the key factors affecting bidirectional reflectance over snow-covered urban canyons.

4.3. Snow Coverage

The impact of snow coverage on the albedo spectrum and bidirectional reflectance within snow-covered urban canyons is illustrated in Figure 13. As snow coverage escalates, the proportion of reflectance contributed by non-snow surfaces decreases accordingly. Snow coverage significantly affects spectral albedo, with increased coverage enhancing reflectance in the visible and near-infrared regions (400–1000 nm), while having a dampening effect on shortwave infrared bands (1600–2200 nm). The influence of varying snow coverage on albedo at around 1.45 µm is minimal, likely due to the low reflection properties of snow and other materials in the 1.4–1.5 µm range, as depicted in Figure 5.

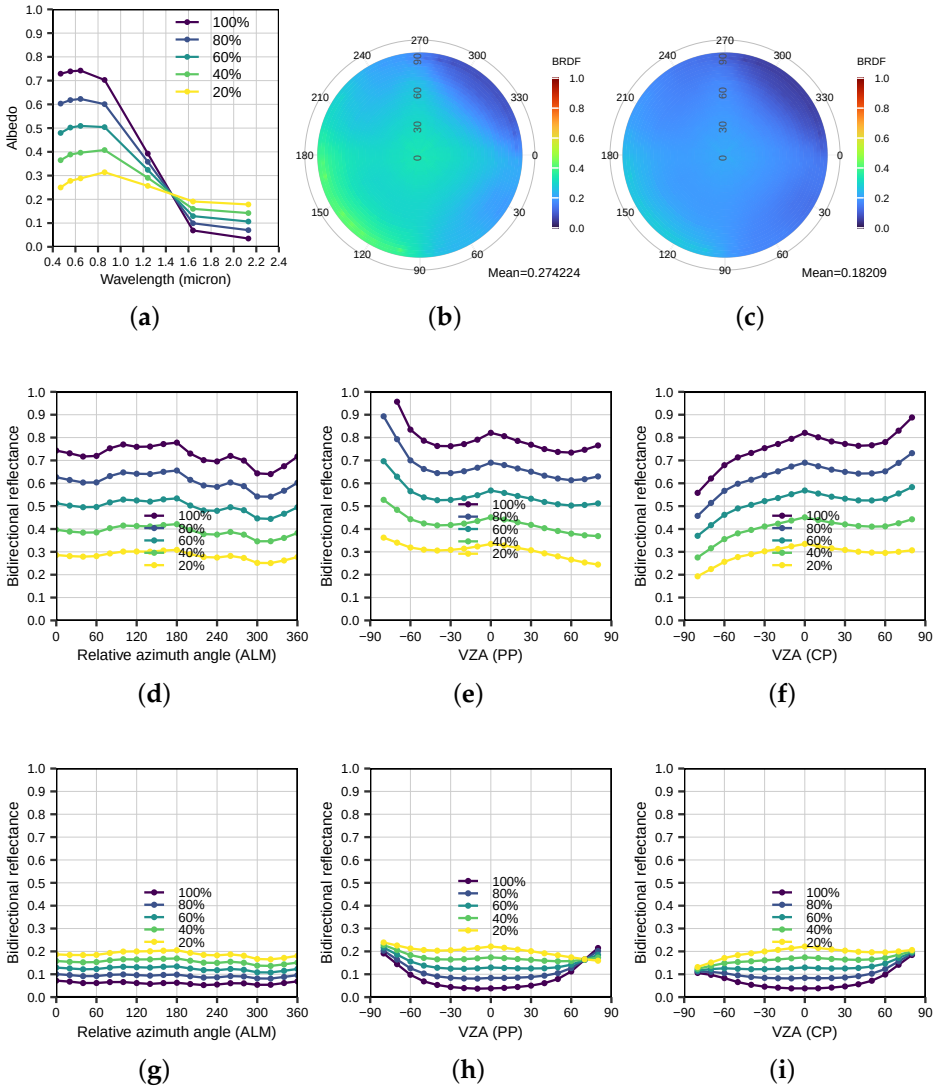

Figure 13. Spectral albedo and BRDF variations over urban canyons with snow coverage varying from 20% to 100%. The negative VZA in the PP represents the direction of the relative azimuth angle of 180° (forward scattering direction), and the negative VZA in the CP represents the direction of the relative azimuth angle of 270°. (**a**) Spectral albedo. (**b**) BRDF distribution at Band 1 with SC = 20%. (**c**) BRDF distribution at Band 6 with SC = 20%. (**d**) ALM reflectance at Band 1. (**e**) PP reflectance at Band 1. (**f**) CP reflectance at Band 1. (**g**) ALM reflectance at Band 6. (**h**) PP reflectance at Band 6. (**i**) CP reflectance at Band 6.

From Figure 13b,c, it is evident that the bidirectional reflectance distribution pattern displays minimal variation. Figure 13d–i illustrate the bidirectional reflectance alterations with increasing snow coverage in the ALM, PP, and CP. While there are no significant impacts on the angular variation of bidirectional reflectance in ALM, PP, and CP at MODIS Band 3, Band 6 exhibits a different pattern. In the PP and CP, bidirectional reflectance at forward and backward scattering angles becomes less sensitive to snow coverage. At smaller SZAs below 30°, bidirectional reflectance is more susceptible to changes in snow coverage. As snow albedo is lower at Band 6 compared to materials like aluminum, roofing felt, asphalt roads, and concrete roads (as depicted in Figure 5), an increase in snow coverage leads to a decrease in reflectance. This overall rise in bidirectional reflectance can be attributed to the interaction between photons and surfaces with higher albedos.

4.4. Snow Grain Size

The spectral variation of surface albedo with respect to snow grain size is illustrated in Figure 14. It is evident that snow grain size exerts a relatively small impact on albedo in the visible and near-infrared regions (400–1000 nm), but its influence becomes pronounced in the shortwave infrared band (1600–2200 nm). The average bidirectional reflectance values for a snow grain size of 5000 µm at Band 1 and Band 6 are 0.554 and 0.112, respectively.

The angular variations of bidirectional reflectance in the ALM, PP, and CP are depicted in Figure 14d–i. In comparison to building coverage, height, and snow cover, snow grain size has a relatively smaller impact on the angular variation pattern at MODIS Band 3, particularly in ALM, PP, and CP. However, this influence is more pronounced at Band 6, and it decreases gradually with larger snow grain sizes. At Band 1, the backscattering reflectance for a 5000 µm input is slightly higher than that for 4000 µm in CP, but this distinction is not observed in Band 6. In Band 1, the backward scattering direction exhibits lower reflectance (0.5–0.6) than the forward scattering direction (around 0.8) in PP. Conversely, at Band 6, the difference in bidirectional reflectance between forward and backward scattering directions is notably reduced.

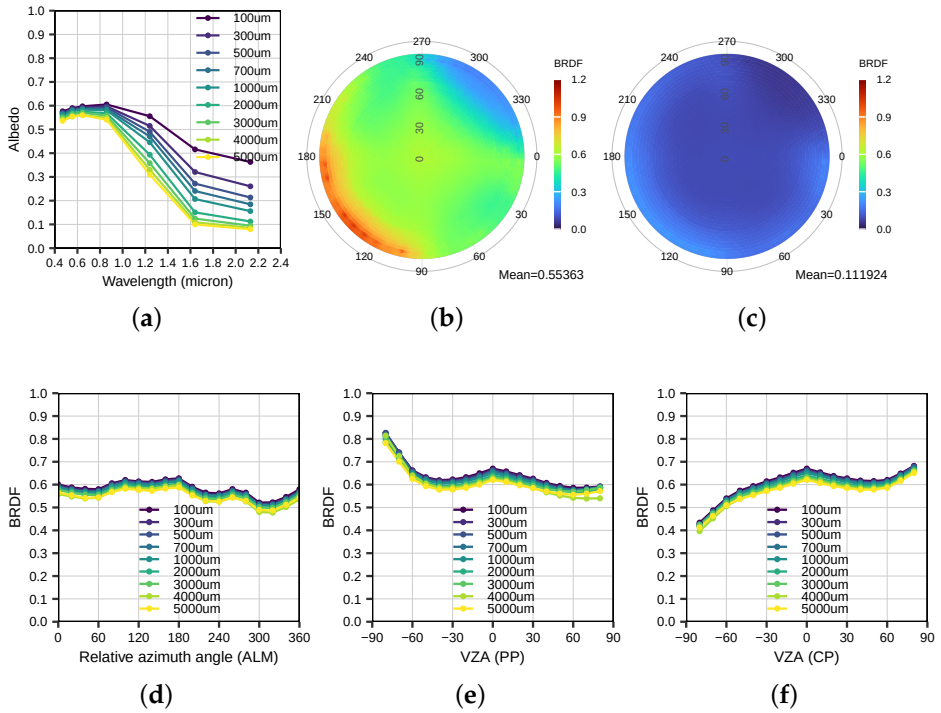

Figure 14. *Cont.*

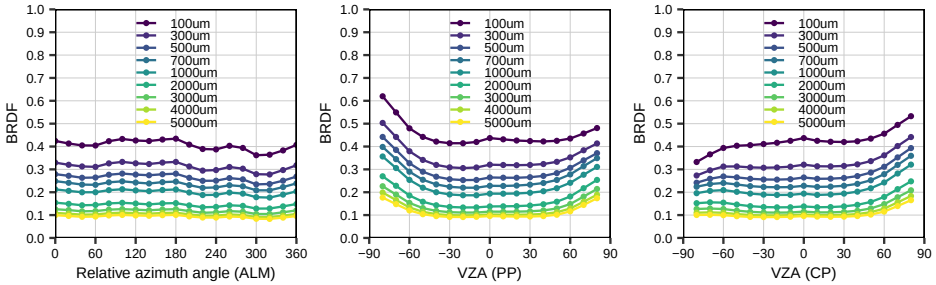

Figure 14. Spectral albedo and BRDF variations over urban canyons with snow grain size varying from 100 to 5000 µm. The negative VZA in the PP represents the direction of the relative azimuth angle of 180° (forward scattering direction), and the negative VZA in the CP represents the direction of the relative azimuth angle of 270°. (**a**) Spectral albedo. (**b**) BRDF distribution at Band 1 with SGS = 5000 µm. (**c**) BRDF distribution at Band 6 with SGS = 5000 µm. (**d**) ALM reflectance at Band 1. (**e**) PP reflectance at Band 1. (**f**) CP reflectance at Band 1. (**g**) ALM reflectance at Band 6. (**h**) PP reflectance at Band 6. (**i**) CP reflectance at Band 6.

4.5. Soot Pollutant Concentration

In Figure 15a, the impact of pollutant concentration on the snow-covered urban canyon's albedo spectrum is evident. The albedo, particularly in the visible and near-infrared (400–1000 nm) bands, is significantly affected, with an average albedo of approximately 0.6 for a concentration of 100 ppb, which doubles to around 645 nm when the concentration is 10^6 ppb. However, this influence is negligible in the shortwave infrared (1600–2200 nm) range. The comparison in Figure 15b,c illustrates that, when a soot pollutant concentration of 10^6 ppb is introduced, the bidirectional reflectance in Band 1 decreases notably across the entire hemisphere, as opposed to Figure 14b, where the difference in Band 6 remains minimal.

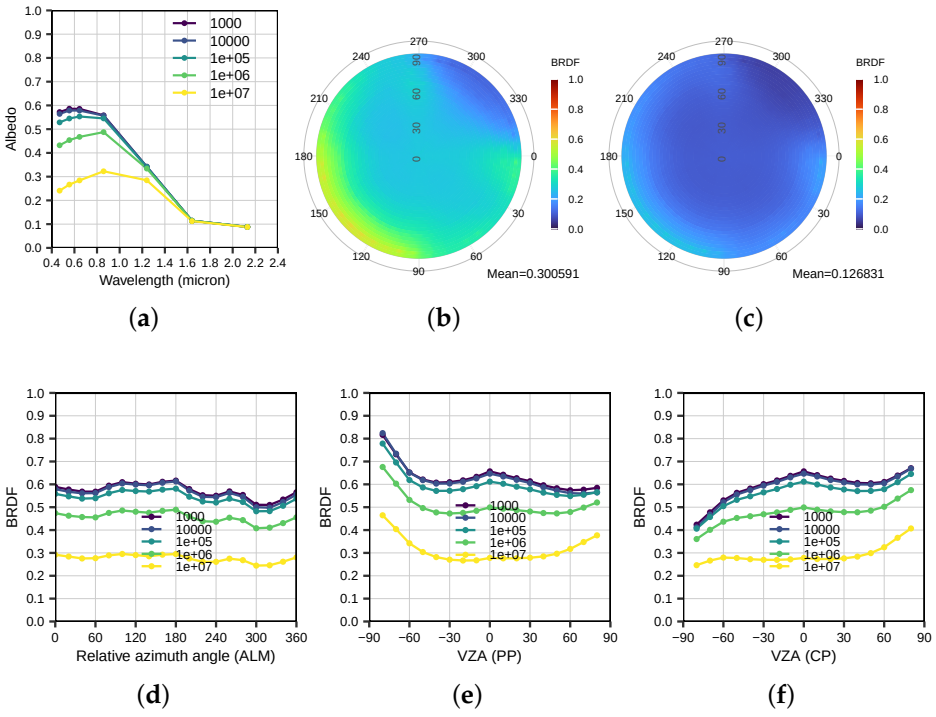

Figure 15. *Cont.*

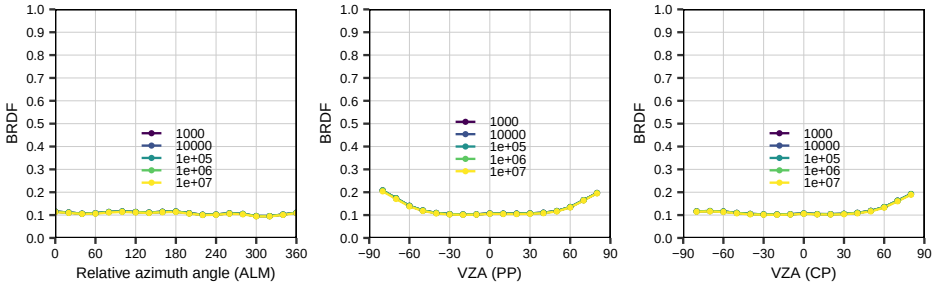

Figure 15. Spectral albedo and BRDF variations over urban canyons with pollutant concentration varying from 10^2 ppb to 10^6 ppb. The negative VZA in the PP represents the direction of the relative azimuth angle of 180° (forward scattering direction), and the negative VZA in the CP represents the direction of the relative azimuth angle of 270°. (**a**) Spectral albedo. (**b**) BRDF distribution at Band 1 with PC = 10^2 ppb. (**c**) BRDF distribution at Band 6 with PC = 10^6 ppb. (**d**) ALM reflectance at Band 1. (**e**) PP reflectance at Band 1. (**f**) CP reflectance at Band 1. (**g**) ALM reflectance at Band 6. (**h**) PP reflectance at Band 6. (**i**) CP reflectance at Band 6.

Figure 15d–i illustrate the bidirectional reflectance changes with varying pollutant concentrations in the ALM, PP, and CP. At Band 6, the reflectance remains virtually unchanged in all three regions as the concentration increases exponentially. In contrast, at Band 1, a noticeable decrease in bidirectional reflectance is observed when the concentration rises from 10^5 ppb to 10^6 ppb. The angular variation pattern at Band 1 shows no significant deviation with the exponential increase in pollutants. The increment in soot concentration leads to a diminishing difference in reflectance between the zenith and nearby VZAs.

4.6. Solar Zenith Angle

Figure 16 demonstrates the effect of SZA on albedo spectrum and bidirectional reflectance. As the SZA rises from 40° to 80°, a slight decrease in spectral reflectance is noted in the visible and infrared bands. The angular distribution of bidirectional reflectance across the hemisphere is shown in Figure 16b,c, with domain-averaged values of 0.598 for Band 1 and 0.141 for Band 6. The increase in SZA leads to enhanced forward scattering, primarily due to the strong forward scattering characteristic of snow at high incident angles [4,8,11].

The angular variation of bidirectional reflectance in ALM, PP, and CP is depicted in Figure 16d–i. The SZA's impact on the ALM's bidirectional reflectance distribution is relatively minor, with similar trends observed in both Band 1 and Band 6. In contrast, the PP exhibits significant changes in bidirectional reflectance with increasing SZA. At low angles (below 60°), backward scattering directions have notably lower reflectance compared to zenith and forward scattering. As the angle increases to 80°, forward and backward scattering directions experience a substantial boost in reflectance, while the reflectance at the zenith direction decreases. A similar pattern is observed in the CP, although the SWIR overall reflectance remains relatively constant. However, a significant rise in backward scattering reflectance is evident in the PP.

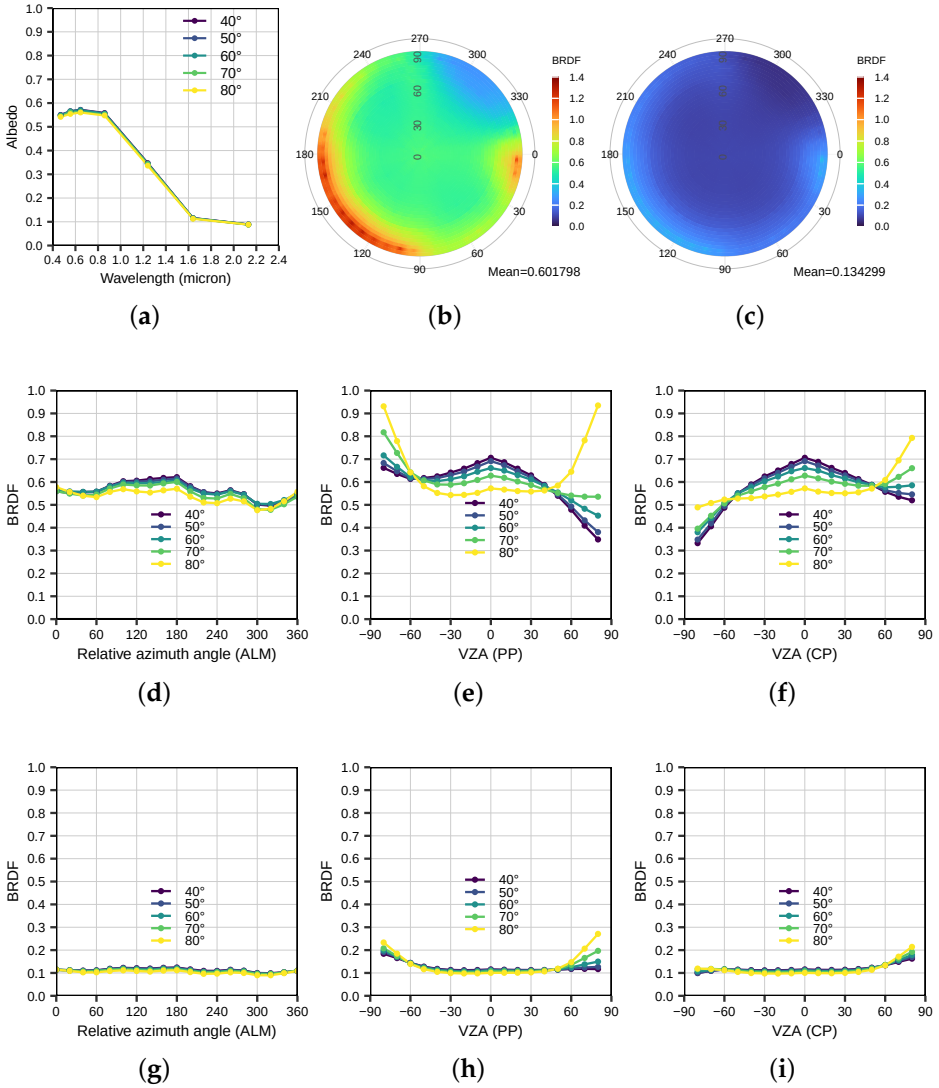

Figure 16. Spectral albedo and BRDF variations over urban canyons with solar zenith angle varying from 40°to 80°. The negative VZA in the PP represents the direction of the relative azimuth angle of 180° (forward scattering direction), and the negative VZA in the CP represents the direction of the relative azimuth angle of 270°. (**a**) Spectral albedo. (**b**) BRDF distribution at Band 1 with SZA = 80°. (**c**) BRDF distribution at Band 6 with SZA = 80°. (**d**) ALM reflectance at Band 1. (**e**) PP reflectance at Band 1. (**f**) CP reflectance at Band 1. (**g**) ALM reflectance at Band 6. (**h**) PP reflectance at Band 6. (**i**) CP reflectance at Band 6.

4.7. Influence of Intertwined Factors on Snow-Covered Urban Albedo

Two scenarios examining the combined effects of various factors on snow-covered urban albedo are explored. Figure 17a–c illustrate the spectral albedo changes with building height and snow coverage. Notably, higher snow coverage and lower building heights result in increased spectral albedo in the visible bands. In contrast, the shortwave infrared band exhibits significantly lower overall albedo, with a slight increase observed as building height and snow coverage decrease. Figure 17d–f highlight the impact of snow grain size and soot pollution concentration. Soot pollution obstructs upward reflection in snow-covered urban canyons. In the visible bands, albedo decreases with larger snow grain size and higher soot pollution. However, in the shortwave infrared band, the primary driver of albedo reduction is the increase in snow grain size, as the influence of soot concentration is negligible due to the low reflectance of snow in this band compared to the visible spectrum and other urban surfaces.

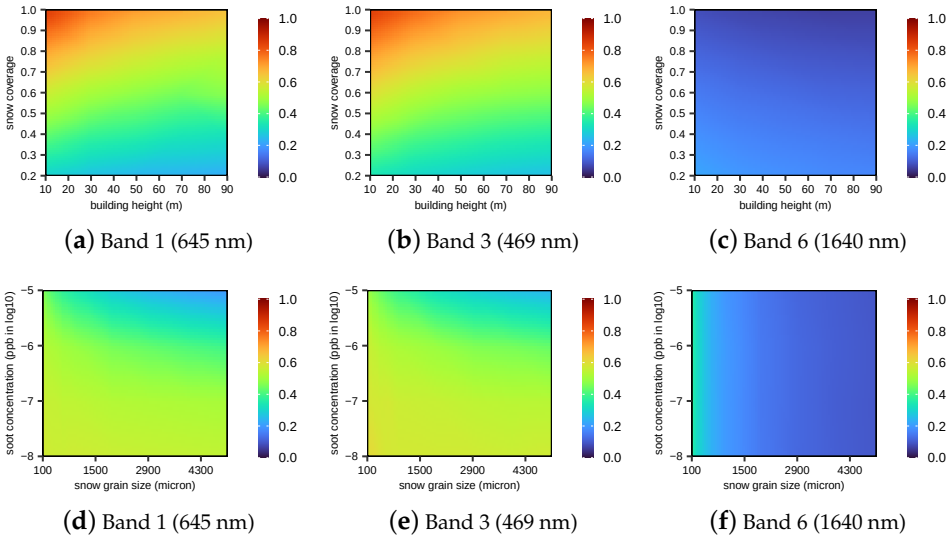

(**a**) Band 1 (645 nm) (**b**) Band 3 (469 nm) (**c**) Band 6 (1640 nm)

(**d**) Band 1 (645 nm) (**e**) Band 3 (469 nm) (**f**) Band 6 (1640 nm)

Figure 17. Spectral albedo with different settings of building heights and snow coverage (**a**–**c**) and of snow grain size and concentration of soot pollution (**d**–**f**).

5. Discussions

Previous research has developed various bidirectional reflectance models for snow-covered environments like mountains and forests. Table 3 provides a concise summary of bidirectional reflectance models applicable to various snow-covered terrains, such as rough snow surfaces, mountainous regions, and forested areas. These models are founded on diverse methodologies, including Monte Carlo ray-tracing techniques [9,26,30,51–53], semi-empirical BRDF approaches [54], and geometric optics [11]. A consistent discovery across these studies is the significant variability in snow's bidirectional reflectance, influenced by the complex interactions with rough surfaces, mountainous terrains, and forests. These interactions with the environment lead to alterations in the BRDF patterns to varying extents. However, a specific model for snow-covered urban canyons is lacking, hindering our understanding of snow's impact on albedo, climate, and remote sensing applications such as aerosol, snow grain, and cloud detection in urban regions. To address this gap, we propose a new snow-covered urban canyon bidirectional reflectance model based on the Monte Carlo ray-tracing technique. The ART model characterizes snow reflectance, while other surfaces use the Lambert model. The findings will advance knowledge about snow's effect on urban canyon anisotropy and inspire further research, including radiation interactions, urban reflectance sensitivity, cloud-snow discrimination, and satellite-based parameter retrieval (e.g., aerosol optical depth, snow coverage, and grain size).

Despite these advancements, limitations persist. The model relies on a simulated urban canyon structure for albedo analysis, suitable for studying snow effects but challenging for capturing the exact angular distribution for a specific district. The model simplifies the surface composition by assuming fixed snow proportions and materials, which may vary with factors like season, location, and study area. Accurate BRDF reproduction requires considering diverse surface characteristics. Additionally, the model assumes equal snow coverage on roofs and ground surfaces, which may not hold in real-world scenarios due to roof shape, slope, and snow removal. While initial validation with flat surfaces and MODIS data suggests the model's effectiveness, a more comprehensive evaluation is hampered by limited multi-angle reflectance data. Future work will involve applying the model to a real urban structure with snow, using UVA technology for land surface parameter estimation and multi-angle observations to enhance model verification and applicability.

Table 3. A brief summary of bidirectional reflectance models for snow-covered regions.

No.	Surface	Method	Reference
1	sastrugi over rough snow	Photometric Roughness Model and a multiple scattering model	Leroux and Fily [51]
2	macroscopic rough snow	Monte Carlo ray-tracing method	Larue et al. [30]
3	small-scale rough snow	Ray-tracing method with photon recollision probability theory	Manninen et al. [53]
4	mountain	Monte Carlo ray-tracing method	Lee et al. [26], Liou et al. [52]
5	mountain	Monte Carlo ray-tracing method	Chu et al. [9]
6	mountain	RTLSR BRDF model	Bertoncini et al. [54]
7	forest	hybrid geometric optical-radiative transfer model	Chen et al. [11]
8	forest	photon recollision probability theory	Jääskeläinen and Manninen [55]
9	urban	Monte Carlo ray-tracing method	This Study

6. Conclusions

This study introduces a novel snow-covered urban canyon bidirectional reflectance model that simulates the impact of urban structures (urban coverage and building height), snow properties (snow coverage, snow grain size, and soot pollutant concentration), and solar zenith angles on the reflectance spectrum and angular distributions across seven MODIS bands (400–2400 nm). We validate the model using three reference cases and real scenarios from MODIS Terra and Aqua data in Harbin, demonstrating its ability to accurately reproduce spectral reflectance in snow-free, fresh snow, and snow melt conditions. A deeper analysis reveals that snow coverage is the primary determinant of albedo spectrum and bidirectional reflectance. Urban coverage, building height, and pollutant concentration have the most significant effect on visible and infrared band reflectance, while snow grain size influences shortwave infrared bands. As building height increases, bidirectional reflectance in the ALM shows less variation at relative azimuth angles between 120° and 180°. Snow coverage changes have minimal impact on the angular variation pattern of directional reflectance in the ALM, PP, and CP. However, at Band 6, bidirectional reflectance at low solar zenith angles (less than 30°) in the PP and CP is more susceptible to snow coverage variations. As snow grain size grows, the bidirectional reflectance at the backward scattering direction in Band 1 (0.5–0.6) is lower than the forward scattering direction (around 0.8) in the PP.

There are several limitations that require attention, including the use of an idealized city model, a fixed ratio of snow and man-made materials for reconstructing surface reflectance, and the assumption of uniform snow coverage on both roofs and the ground. In the future, we plan to apply our numerical model to a realistic 3D urban structure, incorporating more accurate surface reflectance and snow cover configurations to simulate the bidirectional reflectance distribution. This research is anticipated to contribute significantly to the understanding of how snow cover affects the anisotropic reflection characteristics of urban canyons. The outcomes may also catalyze further investigations in associated domains, such as quantifying the radiation interactions between snow and urban surfaces, assessing the sensitivity of urban reflectance to snow and building characteristics, differentiating between clouds and snow, and extracting aerosol optical depth along with snow parameters like coverage, grain size, and pollutant concentration from satellite observations.

Author Contributions: Conceptualization, Q.-X.C. and Z.-Y.G.; methodology, Z.-Y.G.; software, Q.-X.C.; validation, Q.-X.C. and Z.-Y.G.; formal analysis, Q.-X.C. and S.-K.D.; investigation, Q.-X.C. and C.-L.H.; resources, Q.-X.C.; data curation, Q.-X.C.; writing—original draft preparation, Q.-X.C.; writing—review and editing, Q.-X.C. and S.-K.D.; visualization, Q.-X.C. and C.-L.H.; supervision, Q.-X.C. and K.-F.L.; project administration, Q.-X.C. and S.-K.D.; funding acquisition, Q.-X.C. All authors have read and agreed to the published version of the manuscript.

Funding: This research was funded by the China Postdoctoral Science Foundation, grant number No. 2022M720943.

Data Availability Statement: The data used in this study are publicly accessible at EARTHDATA (https://search.earthdata.nasa.gov/search, last accessed 18 April 2024).

Acknowledgments: We thank the MODIS team for providing the data used in this work.

Conflicts of Interest: The authors declare no conflicts of interest.

References

1. Ren, Z.; Fu, Y.; Dong, Y.; Zhang, P.; He, X. Rapid urbanization and climate change significantly contribute to worsening urban human thermal comfort: A national 183-city, 26-year study in China. *Urban Clim.* **2022**, *43*, 101154. [CrossRef]
2. Wang, X.; Meng, X.; Long, Y. Projecting 1 km-grid population distributions from 2020 to 2100 globally under shared socioeconomic pathways. *Sci. Data* **2022**, *9*, 563. [CrossRef] [PubMed]
3. Liou, K.; Takano, Y.; Yang, P. Light absorption and scattering by aggregates: Application to black carbon and snow grains. *J. Quant. Spectrosc. Radiat. Transf.* **2011**, *112*, 1581–1594. [CrossRef]
4. Wu, H.; Liang, S.; Tong, L.; He, T.; Yu, Y. Bidirectional Reflectance for Multiple Snow-Covered Land Types from MISR Products. *IEEE Geosci. Remote Sens. Lett.* **2012**, *9*, 994–998. [CrossRef]
5. Varentsov, M.; Konstantinov, P.; Baklanov, A.; Esau, I.; Miles, V.; Davy, R. Anthropogenic and natural drivers of a strong winter urban heat island in a typical Arctic city. *Atmos. Chem. Phys.* **2018**, *18*, 17573–17587. [CrossRef]
6. Mei, L.; Xue, Y.; de Leeuw, G.; von Hoyningen-Huene, W.; Kokhanovsky, A.A.; Istomina, L.; Guang, J.; Burrows, J.P. Aerosol optical depth retrieval in the Arctic region using MODIS data over snow. *Remote Sens. Environ.* **2013**, *128*, 234–245. [CrossRef]
7. He, C.; Liou, K.N.; Takano, Y. Resolving Size Distribution of Black Carbon Internally Mixed with Snow: Impact on Snow Optical Properties and Albedo. *Geophys. Res. Lett.* **2018**, *45*, 2697–2705. [CrossRef]
8. Mei, L.; Vandenbussche, S.; Rozanov, V.; Proestakis, E.; Amiridis, V.; Callewaert, S.; Vountas, M.; Burrows, J.P. On the retrieval of aerosol optical depth over cryosphere using passive remote sensing. *Remote Sens. Environ.* **2020**, *241*, 111731. [CrossRef]
9. Chu, Q.; Yan, G.; Qi, J.; Mu, X.; Li, L.; Tong, Y.; Zhou, Y.; Liu, Y.; Xie, D.; Wild, M. Quantitative Analysis of Terrain Reflected Solar Radiation in Snow-Covered Mountains: A Case Study in Southeastern Tibetan Plateau. *J. Geophys. Res. Atmos.* **2021**, *126*, e2020JD034294. [CrossRef]
10. Lee, W.L.; Liou, K.N.; Wang, C.C.; Gu, Y.; Hsu, H.H.; Li, J.L.F. Impact of 3-D Radiation-Topography Interactions on Surface Temperature and Energy Budget over the Tibetan Plateau in Winter. *J. Geophys. Res. Atmos.* **2019**, *124*, 1537–1549. [CrossRef]
11. Chen, S.; Xiao, P.; Zhang, X.; Qi, J.; Yin, G.; Ma, W.; Liu, H. Simulating snow-covered forest bidirectional reflectance by extending hybrid geometric optical–radiative transfer model. *Remote Sens. Environ.* **2023**, *296*, 113713. [CrossRef]
12. Ji, W.; Hao, X.; Shao, D.; Yang, Q.; Wang, J.; Li, H.; Huang, G. A New Index for Snow/Ice/Ice-Snow Discrimination Based on BRDF Characteristic Observation Data. *J. Geophys. Res. Atmos.* **2022**, *127*, e2021JD035742. [CrossRef]
13. Gatebe, C.K.; King, M.D. Airborne spectral BRDF of various surface types (ocean, vegetation, snow, desert, wetlands, cloud decks, smoke layers) for remote sensing applications. *Remote Sens. Environ.* **2016**, *179*, 131–148. [CrossRef]
14. Tian, X.; Liu, Q.; Song, Z.; Dou, B.; Li, X. Aerosol Optical Depth Retrieval from Landsat 8 OLI Images over Urban Areas Supported by MODIS BRDF/Albedo Data. *IEEE Geosci. Remote Sens. Lett.* **2018**, *15*, 976–980. [CrossRef]
15. Lin, H.; Li, S.; Xing, J.; He, T.; Yang, J.; Wang, Q. High resolution aerosol optical depth retrieval over urban areas from Landsat-8 OLI images. *Atmos. Environ.* **2021**, *261*, 118591. [CrossRef]
16. Mei, L.; Rozanov, V.; Jiao, Z.; Burrows, J.P. A new snow bidirectional reflectance distribution function model in spectral regions from UV to SWIR: Model development and application to ground-based, aircraft and satellite observations. *ISPRS J. Photogramm. Remote Sens.* **2022**, *188*, 269–285. [CrossRef]
17. Shi, Z.; Xing, T.; Guang, J.; Xue, Y.; Che, Y. Aerosol Optical Depth over the Arctic Snow-Covered Regions Derived from Dual-Viewing Satellite Observations. *Remote Sens.* **2019**, *11*, 891 [CrossRef]
18. Swain, B.; Vountas, M.; Deroubaix, A.; Lelli, L.; Ziegler, Y.; Jafariserajehlou, S.; Gunthe, S.S.; Herber, A.; Ritter, C.; Bösch, H.; et al. Retrieval of aerosol optical depth over the Arctic cryosphere during spring and summer using satellite observations. *Atmos. Meas. Tech.* **2024**, *17*, 359–375. [CrossRef]
19. Kokhanovsky, A.A.; Breon, F.M. Validation of an Analytical Snow BRDF Model Using PARASOL Multi-Angular and Multispectral Observations. *IEEE Geosci. Remote Sens. Lett.* **2012**, *9*, 928–932. [CrossRef]
20. Hsu, N.C.; Lee, J.; Sayer, A.M.; Kim, W.; Bettenhausen, C.; Tsay, S.C. VIIRS Deep Blue Aerosol Products over Land: Extending the EOS Long-Term Aerosol Data Records. *J. Geophys. Res. Atmos.* **2019**, *124*, 4026–4053. [CrossRef]

21. Levy, R.C.; Mattoo, S.; Munchak, L.A.; Remer, L.A.; Sayer, A.M.; Patadia, F.; Hsu, N.C. The Collection 6 MODIS aerosol products over land and ocean. *Atmos. Meas. Tech.* **2013**, *6*, 2989–3034. [CrossRef]
22. Malmros, J.K.; Mernild, S.H.; Wilson, R.; Tagesson, T.; Fensholt, R. Snow cover and snow albedo changes in the central Andes of Chile and Argentina from daily MODIS observations (2000–2016). *Remote Sens. Environ.* **2018**, *209*, 240–252. [CrossRef]
23. Zhang, Y.; Kang, S.; Cong, Z.; Schmale, J.; Sprenger, M.; Li, C.; Yang, W.; Gao, T.; Sillanpää, M.; Li, X.; et al. Light-absorbing impurities enhance glacier albedo reduction in the southeastern Tibetan plateau. *J. Geophys. Res. Atmos.* **2017**, *122*, 6915–6933. [CrossRef]
24. Wang, X.; Shi, T.; Zhang, X.; Chen, Y. An Overview of Snow Albedo Sensitivity to Black Carbon Contamination and Snow Grain Properties Based on Experimental Datasets across the Northern Hemisphere. *Curr. Pollut. Rep.* **2020**, *6*, 368–379. [CrossRef]
25. Cooper, K.D.; Smith, J.A. A Monte Carlo Reflectance Model for Soil Surfaces with Three-Dimensional Structure. *IEEE Trans. Geosci. Remote Sens.* **1985**, *GE-23*, 668–673. [CrossRef]
26. Lee, W.L.; Liou, K.N.; Hall, A. Parameterization of solar fluxes over mountain surfaces for application to climate models. *J. Geophys. Res. Atmos.* **2011**, *116*, D01101. [CrossRef]
27. Jin, S.Y.; Susaki, J. A 3-D Topographic-Relief-Correlated Monte Carlo Radiative Transfer Simulator for Forest Bidirectional Reflectance Estimation. *IEEE Geosci. Remote Sens. Lett.* **2017**, *14*, 964–968. [CrossRef]
28. Kuchiki, K.; Aoki, T.; Niwano, M.; Motoyoshi, H.; Iwabuchi, H. Effect of sastrugi on snow bidirectional reflectance and its application to MODIS data. *J. Geophys. Res. Atmos.* **2011**, *116*. [CrossRef]
29. Xiong, C.; Shi, J. Simulating polarized light scattering in terrestrial snow based on bicontinuous random medium and Monte Carlo ray tracing. *J. Quant. Spectrosc. Radiat. Transf.* **2014**, *133*, 177–189. [CrossRef]
30. Larue, F.; Picard, G.; Arnaud, L.; Ollivier, I.; Delcourt, C.; Lamare, M.; Tuzet, F.; Revuelto, J.; Dumont, M. Snow albedo sensitivity to macroscopic surface roughness using a new ray-tracing model. *Cryosphere* **2020**, *14*, 1651–1672 [CrossRef]
31. Zege, E.; Katsev, I.; Malinka, A.; Prikhach, A.; Heygster, G.; Wiebe, H. Algorithm for retrieval of the effective snow grain size and pollution amount from satellite measurements. *Remote Sens. Environ.* **2011**, *115*, 2674–2685. [CrossRef]
32. Qu, Y.; Liang, S.; Liu, Q.; Li, X.; Feng, Y.; Liu, S. Estimating Arctic sea-ice shortwave albedo from MODIS data. *Remote Sens. Environ.* **2016**, *186*, 32–46. [CrossRef]
33. Kokhanovsky, A.; Lamare, M.; Di Mauro, B.; Picard, G.; Arnaud, L.; Dumont, M.; Tuzet, F.; Brockmann, C.; Box, J.E. On the reflectance spectroscopy of snow. *Cryosphere* **2018**, *12*, 2371–2382. [CrossRef]
34. Shui, T.; Liu, J.; Xiao, Y.; Shi, L. Effects of snow cover on urban surface energy exchange: Observations in Harbin, China during the winter season. *Int. J. Climatol.* **2019**, *39*, 1230–1242. [CrossRef]
35. Fu, D.L.; Zhang, W.; Xing, Y.; Li, H.; Wang, P.; Li, B.; Shi, X.; Jinxiang, Z.; Yabo, S.; Thapa, S.; et al. Impacts of maximum snow albedo and land cover changes on meteorological variables during winter in northeast China. *Atmos. Res.* **2021**, *254*, 105449. [CrossRef]
36. Chen, Q.X.; Shen, W.X.; Yuan, Y.; Tan, H.P. Verification of aerosol classification methods through satellite and ground-based measurements over Harbin, Northeast China. *Atmos. Res.* **2019**, *216*, 167–175. [CrossRef]
37. Chen, Q.; Yuan, Y.; Huang, X.; He, Z.; Tan, H. Assessment of column aerosol optical properties using ground-based sun-photometer at urban Harbin, Northeast China. *J. Environ. Sci.* **2018**, *74*, 50–57. [CrossRef] [PubMed]
38. Cheng, Y.; Zhong, Y.-J.; Liu, J.-M.; Cao, X.-B.; Zhang, Q.; He, K.-B. Response of Harbin aerosol to latest clean air actions in China. *J. Hazard. Mater.* **2024**, *467*, 133728. [CrossRef] [PubMed]
39. Skakun, S.; Justice, C.; Vermote, E.; Roger, J.C. Transitioning from MODIS to VIIRS: An analysis of inter-consistency of NDVI data sets for agricultural monitoring. *Int. J. Remote Sens.* **2018**, *39*, 971–992. [CrossRef] [PubMed]
40. Salomon, J.; Schaaf, C.; Strahler, A.; Gao, F.; Jin, Y. Validation of the MODIS bidirectional reflectance distribution function and albedo retrievals using combined observations from the aqua and terra platforms. *IEEE Trans. Geosci. Remote Sens.* **2006**, *44*, 1555–1565. [CrossRef]
41. Schaaf, C.B.; Liu, J.; Gao, F.; Strahler, A.H. Aqua and Terra MODIS Albedo and Reflectance Anisotropy Products. In *Land Remote Sensing and Global Environmental Change: NASA's Earth Observing System and the Science of ASTER and MODIS*; Ramachandran, B., Justice, C.O., Abrams, M.J., Eds.; Springer: New York, NY, USA, 2011; pp. 549–561. [CrossRef]
42. Li, X.; Strahler, A.H. Geometric-optical bidirectional reflectance modeling of the discrete crown vegetation canopy: Effect of crown shape and mutual shadowing. *IEEE Trans. Geosci. Remote Sens.* **1992**, *30*, 276–292. [CrossRef]
43. Friedl, M.; McIver, D.; Hodges, J.; Zhang, X.; Muchoney, D.; Strahler, A.; Woodcock, C.; Gopal, S.; Schneider, A.; Cooper, A.; et al. Global land cover mapping from MODIS: Algorithms and early results. *Remote Sens. Environ.* **2002**, *83*, 287–302. [CrossRef]
44. Abercrombie, S.P.; Friedl, M.A. Improving the Consistency of Multitemporal Land Cover Maps Using a Hidden Markov Model. *IEEE Trans. Geosci. Remote Sens.* **2016**, *54*, 703–713. [CrossRef]
45. Hansen, M.C.; DeFries, R.S.; Townshend, J.R.; Sohlberg, R. Global land cover classification at 1 km spatial resolution using a classification tree approach. *Int. J. Remote Sens.* **2000**, *21*, 1331–1364. [CrossRef]
46. Kokhanovsky, A.; Aoki, T.; Hachikubo, A.; Hori, M.; Zege, E. Reflective properties of natural snow: Approximate asymptotic theory versus in situ measurements. *IEEE Trans. Geosci. Remote Sens.* **2005**, *43*, 1529–1535. [CrossRef]
47. Kokaly, R.; Clark, R.; Swayze, G.; Livo, K.; Hoefen, T.; Pearson, N.; Wise, R.; Benzel, W.; Lowers, H.; Driscoll, R. *USGS Spectral Library Version 7*; USGS: Reston, VA, USA , 2017. [CrossRef]

48. Pincus, R.; Evans, K.F. Computational Cost and Accuracy in Calculating Three-Dimensional Radiative Transfer: Results for New Implementations of Monte Carlo and SHDOM. *J. Atmos. Sci.* **2009**, *66*, 3131–3146. [CrossRef]
49. Qi, J.; Xie, D.; Yin, T.; Yan, G.; Gastellu-Etchegorry, J.P.; Li, L.; Zhang, W.; Mu, X.; Norford, L.K. LESS: LargE-Scale remote sensing data and image simulation framework over heterogeneous 3D scenes. *Remote Sens. Environ.* **2019**, *221*, 695–706. [CrossRef]
50. Chen, Y.; Hall, A.; Liou, K.N. Application of three-dimensional solar radiative transfer to mountains. *J. Geophys. Res. Atmos.* **2006**, *111*. [CrossRef]
51. Leroux, C.; Fily, M. Modeling the effect of sastrugi on snow reflectance. *J. Geophys.-Res.-Planets* **1998**, *103*, 25779–25788. [CrossRef]
52. Liou, K.N.; Lee, W.L.; Hall, A. Radiative transfer in mountains: Application to the Tibetan Plateau. *Geophys. Res. Lett.* **2007**, *34*. [CrossRef]
53. Manninen, T.; Anttila, K.; Jaaskelainen, E.; Riihela, A.; Peltoniemi, J.; Raisanen, P.; Lahtinen, P.; Siljamo, N.; Tholix, L.; Meinander, O.; et al. Effect of small-scale snow surface roughness on snow albedo and reflectance. *Cryosphere* **2021**, *15*, 793–820. [CrossRef]
54. Bertoncini, A.; Aubry-Wake, C.; Pomeroy, J.W. Large-area high spatial resolution albedo retrievals from remote sensing for use in assessing the impact of wildfire soot deposition on high mountain snow and ice melt. *Remote Sens. Environ.* **2022**, *278*, 113101. [CrossRef]
55. Jääskeläinen, E.; Manninen, T. The effect of snow at forest floor on boreal forest albedo diurnal and seasonal variation during the melting season. *Cold Reg. Sci. Technol.* **2021**, *185*, 103249. [CrossRef]

Disclaimer/Publisher's Note: The statements, opinions and data contained in all publications are solely those of the individual author(s) and contributor(s) and not of MDPI and/or the editor(s). MDPI and/or the editor(s) disclaim responsibility for any injury to people or property resulting from any ideas, methods, instructions or products referred to in the content.